Available online at www.sciencedirect.com
ScienceDirect
International Journal of Heat and Mass Transfer 50 (2007) 335–347
International Journal of HEAT and MASS TRANSFER
www.elsevier.com/locate/ijhmt

Effect of stable-density stratification on counter gradient flux of a homogeneous shear flow

Oaki Iida *, Yasutaka Nagano

Department of Mechanical Engineering, Nagoya Institute of Technology, Gokiso-cho, Showa-ku, Nagoya 466-8555, Japan

Received 10 January 2006; received in revised form 10 May 2006
Available online 1 September 2006

Abstract

We performed direct numerical simulations of homogeneous shear flow under stable-density stratification to study the buoyancy effects on the heat and momentum transfer. These numerical data were compared with those of a turbulent channel flow to investigate the similarity between the near-wall turbulence and the homogeneous shear flow. We also investigated the generation mechanism of the persistent CGFs (counter gradient fluxes) appearing at the higher wavenumbers of the cospectrum, and lasting over a long time without oscillation. Spatially, the persistent CGFs are associated with the longitudinal vortical structure, which is elongated in the streamwise direction and typically observed in both homogeneous shear flow and near-wall turbulence. The CGFs appear at both the top and bottom of this longitudinal vortical structure, and expand horizontally with an increase in the Richardson number. It was found that the production and turbulent-diffusion terms are responsible for the distribution of the Reynolds shear stress including the persistent CGFs. The buoyancy term, combined with the swirling motion of the vortex, contributes to expand the persistent CGF regions and decrease the down gradient fluxes.

Keywords: Counter gradient flux; Stable-density stratification; Vortical structure; DNS

1. Introduction

The stratified flow is defined as a flow primarily in the horizontal direction that is affected by a vertical variation of the density [1]. Such flows are very important in geophysics as well as engineering. Not only in many important engineering flows, but also in geophysical flows, turbulent momentum and heat transports occur in the near-wall region under the presence of stable-density stratification. That region's longitudinal streamwise vortical structure makes a significant contribution to the momentum and heat transfer [2,3]. This longitudinal vortical structure is elongated in the streamwise direction and characterized by the streamwise vortical motion and intense streamwise vorticity.

Recently, that same vortical structure was observed in the homogeneous shear flow as well in the wall turbulence [4]; similar strain rates, which affect the redistribution and energy transfer of the Reynolds stresses as well as their production, were found to be imposed on the vortical structure of both the homogeneous shear flow and wall turbulence. Hence, similar buoyancy effects may be observed on the heat and momentum transfer associated with the vortical structure, although no quantitative comparison has been made between the homogeneous shear flow and near-wall turbulence under stable-density stratification.

As far as stable-density stratification is concerned, many numerical and experimental studies have been performed on homogeneous shear flow, and counter-gradient fluxes (CGFs) have been investigated there in detail [4–10].

The CGFs represent the Reynolds shear stresses which transfer the momentum to enhance the imposed mean shear and contribute to the negative production of turbulent kinetic energy k, and hence they are local phenomena in time or space [12]. Under stable density stratification, however, the CGFs may become quantitatively more important

* Corresponding author. Tel./fax: +81 52 735 5347.
E-mail address: iida.oaki@nitech.ac.jp (O. Iida).

0017-9310/$ - see front matter © 2006 Elsevier Ltd. All rights reserved.
doi:10.1016/j.ijheatmasstransfer.2006.06.022

Nomenclature

D_κ	spectrum of dissipation rate ε
E_κ	energy spectrum of turbulent kinetic energy k
E_{12}	cospectrum of velocity fluctuations u_1 and u_2
E^*_{12}	E_{12} normalized by the spatial average of the Reynolds shear stress
g	gravitational acceleration
II	second invariant of deformation tensor
$II_{\mathrm{r.m.s.}}$	root-mean-square value of II
k	turbulent kinetic energy, $\overline{u_i u_i}/2$
k_0	initial turbulent kinetic energy
L_i	side of computational region in the ith direction
$L_{ij,k}$	integral scale of kth direction, $\int_0^{L_k/2} \overline{u_i(x_k)u_j(x_k+r_k)}/\sqrt{\overline{u_i^2}}\sqrt{\overline{u_j^2}}dr_k$
N	buoyancy frequency, $\sqrt{g\beta S_\theta}$
Pr	the Prandtl number
p	pressure (see Eq. (10) for detail definition)
p_{r}	rapid pressure (see Eq. (11) for detail definition)
p_{s}	slow pressure (see Eq. (12) for detail definition)
q	reference turbulent velocity, $\sqrt{\overline{u_i u_i}}$
Re_{t}	turbulent Reynolds number
Ri	gradient Richardson number
R_{12}	cross correlation between u_1 and u_2, $R_{12} = -\overline{u_1 u_2}/\sqrt{\overline{u_1^2}}\sqrt{\overline{u_2^2}}$
$R_{2\theta}$	cross correlation between θ and u_2, $R_{2\theta} = -\overline{u_2\theta}/\sqrt{\overline{u_2^2}}\sqrt{\overline{\theta^2}}$
r_{e}	radius of vortex
S	mean velocity gradient
S_{r}	reference mean velocity gradient
S_ρ	mean density gradient
S_θ	mean temperature gradient
S^*	shear rate number
s_{ij}	strain rate tensor
t	time
$\widetilde{U}_i$	instantaneous velocity in x_i-direction
$\overline{U}_i$	mean velocity in x_i-direction
u_i	fluctuating velocity in x_i-direction
x_1, x_2, x_3	streamwise, vertical and spanwise directions
β	volumetric expansion coefficient
γ	diffusivity of density and temperature
ε	dissipation rate of turbulent kinetic energy
η	Kolmogorov scale
τ	tilting angle of longitudinal vortical structure (see Fig. 8 for detail)
κ	three-dimensional wavenumber, $\sqrt{\kappa_i\kappa_i}$
κ_i	wavenumber of ith direction
κ_η	Kolomogorov wavenumber, $2\pi/\eta$
θ	temperature fluctuation
ν	kinematic viscosity
ρ	density
$\tilde{\rho}$	instantaneous density
ρ_0	reference density
ω_i	ith component of vorticity vector
$\langle\ \rangle$	conditionally averaged value
$\overline{(\ )}$	volume averaged value

in comparison to the case without it because of a significant decrease in the down gradient fluxes (DGFs).

Webster [5] measured the data of stationary homogeneous shear flow under stable stratification. His data have subsequently often been used for a comparison to check the validity of numerical and experimental data. Gerz et al. [6] performed numerical simulations on stratified homogeneous shear flow, and studied the generation mechanism of the CGFs appearing in a high-Prandtl-number flow, though this is mostly explained by the linear process. The linearly generated CGFs were confirmed in the experimental study of a homogeneous shear flow [7].

Recently, the rapid distortion theory, RDT, was found to predict the CGFs in a homogeneous shear flow as well as a homogeneous decaying turbulence [8]. The RDT can predict the oscillation motion of both the turbulent heat flux and the Reynolds shear stress at the large Richardson number.

There are some studies, however, indicating that the contribution of nonlinear terms to the CGFs cannot be negligible. Holt et al. [9], presenting the close association between CGFs and hairpin vortices, reported that the swirling motion of the vortex contributed to generating the CGFs, and that the nonlinear convective process was responsible for CGF generation. They also showed that these nonlinear CGFs persistently appear at high wavenumbers even without buoyancy. They found, however, that at the very large Richardson number, the nonlinear effects became negligible, and that the CGFs appeared over all the wavenumbers of the cospectrum, which is predictable by the RDT.

In [10], the CGFs appearing at high wavenumbers were named as the persistent CGFs, and they conjectured that such persistent CGFs were generated because the Reynolds shear stress produced by the vortical swirling motion rapidly cascaded into the higher wavenumbers; the molecular diffusion could not dissipate the Reynolds shear stress before emergence of the CGFs. However, their assumption has been confirmed by neither the experimental nor the numerical results.

Persistent CGFs are generated not only in a homogeneous shear flow [9–11], but also in a boundary layer [13] and mixing layer [14], indicating that these CGFs appear in almost all the turbulent shear flows. Hence, we should pay closer attention to persistent CGFs, and their association with the vortical structure.

The objective of this study is to clarify the effect of stable-density stratification on the turbulent heat and mass transfer. Not only persistent CGFs, but also DGFs are associated with the vortical structure, which is commonly observed in homogeneous shear flow and near-wall turbulence. Hence, we discuss the similarity of the stratified effects on turbulent heat and mass transfer between homogeneous shear flow and near-wall turbulence. The generation mechanism of persistent CGFs and the effects of buoyancy on the CGFs and DGFs are then studied by investigating the transport mechanism around the longitudinal vortical structure.

2. Numerical methods and dynamical parameters

We performed both DNS and RDT analyses of a homogeneous shear flow at a low Reynolds number with grid points of $64 \times 64 \times 64$ and $128 \times 128 \times 128$ in the streamwise (x_1), normal (x_2) and spanwise (x_3) directions. Gravitational acceleration g is imposed on the x_2 direction.

The governing equations are the Boussinesq form of Navier–Stokes equations and an equation for the transport of density, which are written as

$$\frac{\partial \widetilde{U}_i}{\partial x_i} = 0, \tag{1}$$

$$\frac{\partial \widetilde{U}_i}{\partial t} + \widetilde{U}_j \frac{\partial \widetilde{U}_i}{\partial x_j} = -\frac{1}{\rho_0}\frac{\partial \widetilde{P}}{\partial x_i} - \frac{g}{\rho_0}\rho\delta_{i2} + \nu\frac{\partial^2 \widetilde{U}_i}{\partial x_j \partial x_j}, \tag{2}$$

$$\frac{\partial \tilde{\rho}}{\partial t} + \widetilde{U}_j \frac{\partial \tilde{\rho}}{\partial x_j} = \gamma\frac{\partial^2 \tilde{\rho}}{\partial x_j \partial x_j}, \tag{3}$$

where $\tilde{}$ represents the instantaneous value and $\widetilde{U}$, $\tilde{p}$, and $\tilde{\rho}$ represent the instantaneous velocity, pressure and density, respectively. ν and γ are kinematic viscosity and diffusivity, respectively. Instantaneous density $\tilde{\rho}$, constant reference density ρ_0, and fluctuating density ρ are associated as $\tilde{\rho} = \rho_0 + S_\rho x_2 + \rho$, where S_ρ is the constant mean density gradient. A uniform shear flow is also introduced by setting the mean velocity $\overline{U}_i = (Sx_2, 0, 0)$, where S is the imposed mean shear rate. The instantaneous velocity can be associated with the mean and fluctuating velocities as $\widetilde{U}_i = \overline{U}_i + u_i$.

The equations for the fluctuations are written as

$$\frac{\partial u_j}{\partial x_j} = 0, \tag{4}$$

$$\frac{\partial u_i}{\partial t} + \overline{U}_j\frac{\partial u_i}{\partial x_j} + u_j\frac{\partial u_i}{\partial x_j} + Su_2\delta_{i1} = -\frac{1}{\rho_0}\frac{\partial p}{\partial x_i} - \frac{\rho}{\rho_0}g\delta_{i2} + \nu\frac{\partial^2 u_i}{\partial x_j \partial x_j}, \tag{5}$$

$$\frac{\partial \rho}{\partial t} + \overline{U}_j\frac{\partial \rho}{\partial x_j} + u_j\frac{\partial \rho}{\partial x_j} + S_\rho u_2 = \gamma\frac{\partial^2 \rho}{\partial x_j \partial x_j}. \tag{6}$$

The buoyancy term $g\rho/\rho_0$ is converted into $-g\beta\theta$ by the Boussinesq approximation, where β and θ represent the thermal expansion rate and temperature fluctuations, respectively. In the following, all velocity fluctuations and length scales in this study are non-dimensionalized by $\sqrt{S_r\nu/2}$ and $\sqrt{2\nu/S_r}$, where S_r represents the reference mean velocity gradient, and S/S_r is different in the numerical simulation of the different shear rate. Temperature is non-dimensionalized, however, by $S_\theta/4$ and $\sqrt{2\nu/S_r}$, where S_θ represents the mean temperature gradient.

Spectral accuracy in spatial discretization can be obtained by use of the periodic boundary conditions and the coordinate transformation developed by Rogallo [15]. The sides of the computational region L_1, L_2, and L_3 are $4\pi\sqrt{S_r/2\nu}(=380)$, $2\pi\sqrt{S_r/2\nu}$, and $2\pi\sqrt{S_r/2\nu}$ in the x_1, x_2 and x_3 directions, respectively.

We artificially generated isotropic turbulence and decayed it until the energy spectrum almost reached the equilibrium state. We then used this decaying isotropic turbulence as the initial condition for the homogeneous shear flow. With this method, we can more rapidly obtain an equilibrium state. The initial energy spectrum for decaying isotropic turbulence is determined as

$$E(k) = A\kappa^2 \exp\frac{-\kappa^2}{B^2}. \tag{7}$$

In cases C representing the numerical simulations of coarse grids, the constants A and B are set to be 1400 and 0.265, respectively; in case F representing the case of finer grids, they are set to be 30,000 and 0.265, respectively. When the turbulent Reynolds number of this isotropic turbulence becomes $Re_t(=q^4/\varepsilon\nu) = 66$ (260 for cases F), this decaying turbulence is used as the initial condition for the homogeneous shear flow of cases C.

Details of the numerical parameters used in these studies are listed in Table 1, where the initial values of the Reynolds number and the shear rate parameters are included. In each case, we did several numerical simulations by systematically changing the shear rate parameters (Sq^2/ϵ) and the Richardson numbers $Ri(=N^2/S^2 = g\beta S_\theta/S^2)$. However, the Prandtl number $Pr = \nu/\gamma$ is set to be 0.71 in all cases.

Direct numerical simulation is carried out with a pseudo-spectral code developed by Rogallo [15] for a homogeneous shear flow. The remeshing of the grid system is used to avoid its distortion at $St = 1, 3, 5, \ldots, 19$. The resulting alias error is removed by the combination of a phase shift and a truncation of high wavenumbers. The RDT is also computed by the same DNS code.

Table 1
Flow conditions

Case	C1	C2	C3	F3
Grids points	64^3			128^3
$Re_t = q^4/\epsilon\nu$	66			260
$S^* = Sq^2/\epsilon$	6.9	14	27	28
S/S_r	0.025	0.5	1	1
Ri	0, 0.1, 0.16, 0.18, 0.2, 0.3, 0.4, 0.5			
Pr	0.71			

In all cases, both the energy and dissipation spectra decay sufficiently at the high wavenumbers. Moreover, the longitudinal integral scale of the streamwise velocity is much larger than the longitudinal length of the vortex we will discuss in detail.

3. Results and discussion

3.1. Correlation between homogeneous flow and wall turbulence under density stratification

The time development of the turbulent kinetic energy k of case F3 is shown in Fig. 1. This is usually predicted by the RDT. When the Richardson number is below 0.2, k increases with time, while at the Richardson number larger than 0.2, k decreases with time. As indicated by Holt et al. [9], there is a stationary Richardson number where all the terms of k budget balance, and both energy and dissipation spectra remain mostly unchanged with time as shown in Fig. 2. It is also noted in Fig. 2 that both the energy and dissipation are well resolved in this simulation. This stationary Richardson number was first identified by Holt et al. [9], and then Shih et al. [16] and Jacobitz et al. [17] found that at the condition of a low Reynolds number, the stationary Richardson number is affected by both the Reynolds number and shear rate parameter.

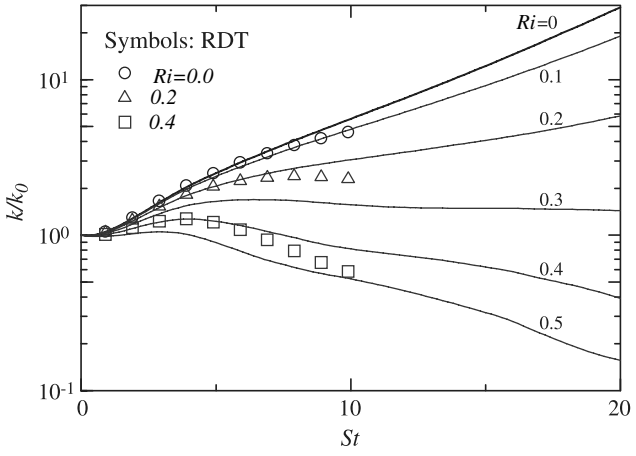

Fig. 1. Time development of normalized turbulent kinetic energy k/k_0 at different Richardson numbers in case F3.

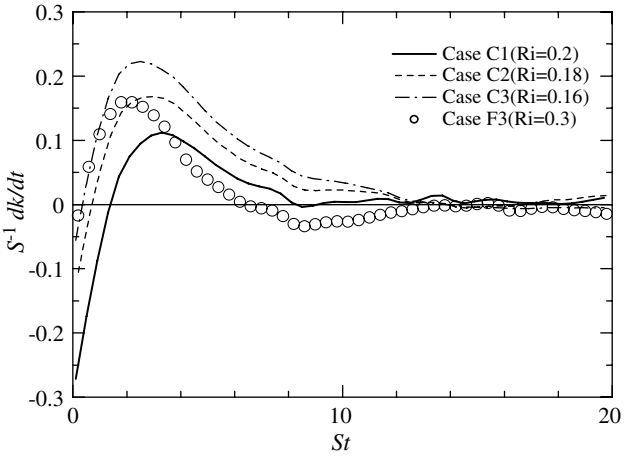

Fig. 3. Time development of unsteady terms at stationary Richardson number in all cases.

The stationary Richardson number in each case is determined by time development of the unsteady term of the k budget, which is shown in Fig. 3. In all cases, the unsteady term finally converges to zero, indicating that we chose the valid stationary Richardson number for every shear rate.

To reduce their dependence on St, we determined the reference values of both the normalized Reynolds shear stress and turbulent heat flux (R_{12} and $R_{2\theta}$) at the stationary

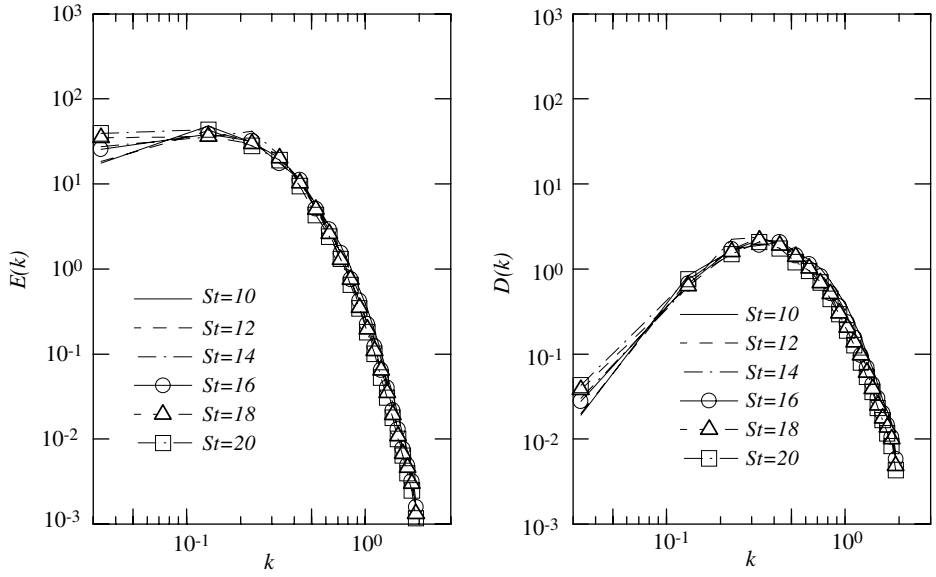

Fig. 2. Time development of three-dimensional energy and dissipation spectra at stationary Richardson numbers in case F3.

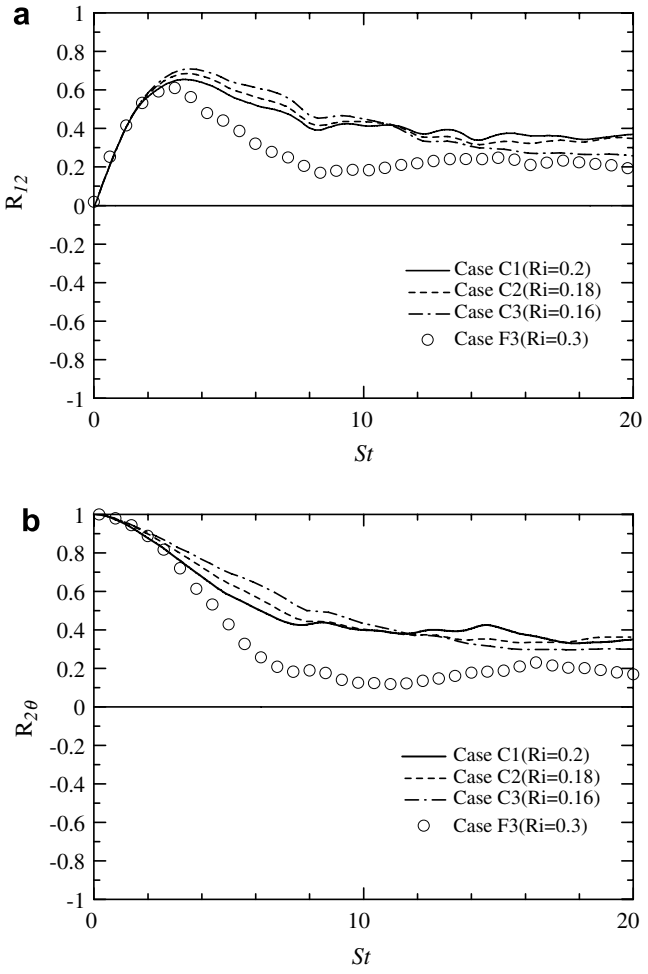

Fig. 4. (a) Time development of R_{12} in all cases, (b) time development of $R_{2\theta}$ in all cases; at $St = 19$, R_{12} takes 0.21 ($Ri = 0.3$), 0.354 ($Ri = 0.2$), 0.349 ($Ri = 0.18$), 0.256 ($Ri = 0.16$), while $R_{2\theta}$ takes 0.19 ($Ri = 0.3$), 0.337 ($Ri = 0.2$), 0.362 ($Ri = 0.18$), 0.299 ($Ri = 0.16$).

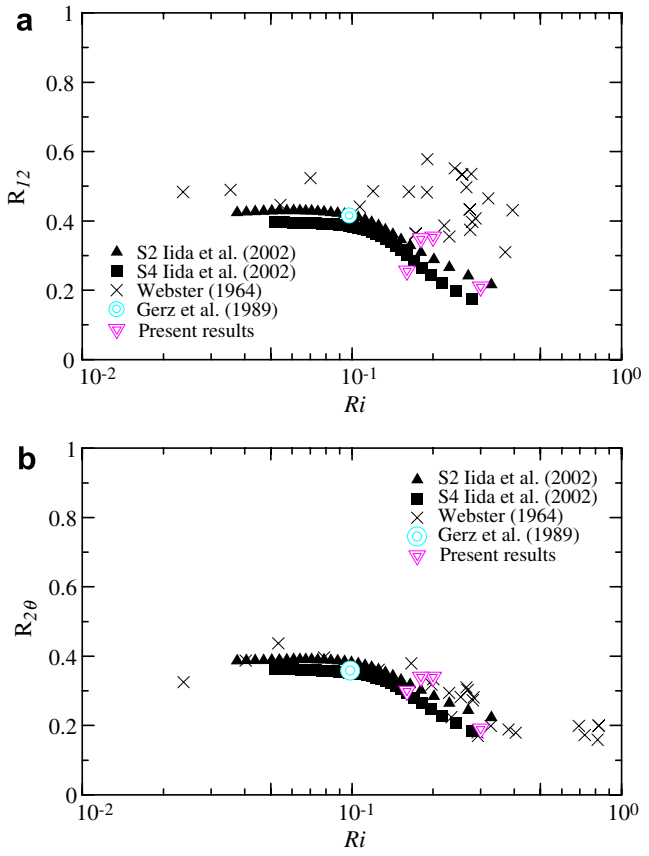

Fig. 5. (a) Richardson number effect on R_{12}, (b) Richardson number effect on $R_{2\theta}$.

Richardson numbers. The time development of R_{12} and $R_{2\theta}$ is shown in Fig. 4(a) and (b), where they are plotted at the stationary Richardson numbers. In the very early period of this calculation, both change drastically, though they approach stationary values with time. Thus, we evaluated them at $St = 19$ as the reference values at the stationary Richardson numbers; the chosen time does not have much influence as long as the flow is stationary.

Finally, R_{12} and $R_{2\theta}$ are compared with those of the turbulent channel flow [18] and other homogeneous shear flows to show the validity of our results (see Fig. 5(a) and (b)). The closed symbols represent the data of the buffer and the logarithmic regions of stratified channel flow; the open symbols represent the results of homogeneous shear flow at the stationary Richardson number.

Not only our data but also those of Gerz et al. [6] show good agreement with the channel data in both R_{12} and $R_{2\theta}$; the data of Gerz et al. are almost at the stationary Richardson number. In particular, the dots of $R_{2\theta}$ are mostly plotted on a single curve, including the experimental results of Webster. Hence, the normalized turbulent heat flux is particularly dependent on the Richardson numbers.

The dependence of both the Reynolds shear stress and turbulent heat flux on the Richardson number is also indicated by Komori et al. [19], though their results are on the near free-surface region where the mean shear rate is weak, and the longitudinal vortical structure may not be observed.

3.2. Mechanisms of persistent CGFs

Fig. 6(a) and (b) shows the time development of the cospectra of u_1 and u_2 in case C2. It is noted that the CGFs appear at the high wavenumbers after $St = 6$. After $St = 10$, the flow almost reaches the equilibrium state, and the persistent CGFs continue to appear at higher wavenumbers as previously observed [9–11]. These fluxes were first identified as persistent CGFs by Gerz et al. [10], and have been reported in the various shear flow phenomena such as the mixing and boundary layers as well as experimental and numerical homogeneous shear flows.

They are more markedly observed in the cases of the higher Reynolds number with finer resolution, indicating that persistent CGFs are not numerical errors. Fig. 7 shows the cospectra of u_1 and u_2 in case F3, which are non-dimensionalized by the Kolmogorov scale $\eta = (\nu^3/\epsilon)^{1/4}$ and the

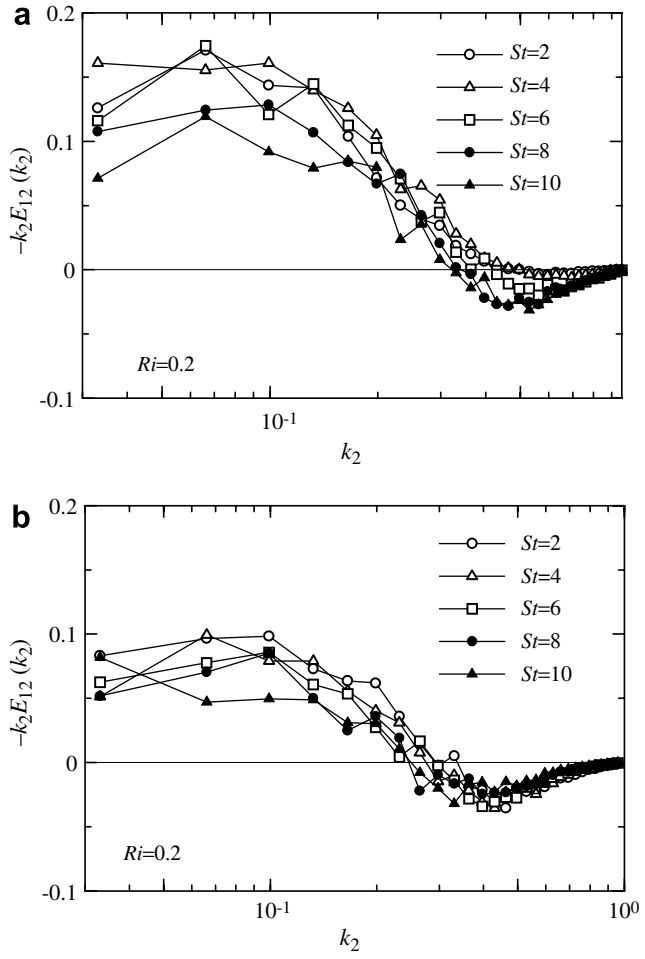

Fig. 6. Time development of cospectrum of u_1 and u_2 in case C2 of $Ri = 0.2$, (a) $St = 2$–10, (b) $St = 10$–20.

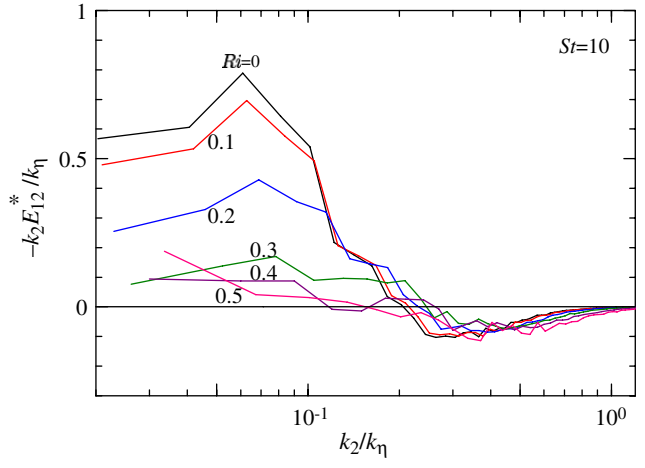

Fig. 7. Richardson number effect on normalized cospectrum of u_1 and u_2 at $St = 10$ in case F3; E_{12} is normalized by the Reynolds shear stress averaged in the entire regions of $-uv < 0$ (CGF), while wavenumber κ_2 is normalized by the Kolmogorov scale.

average of the CGFs over the entire flow. With an increase in the Richardson number, decreases in the DGFs are marked in comparison to those in the CGFs. It is also noted that the energy spectra at high wavenumbers converge into a single curve, strongly indicating that the structure of the persistent CGFs does not change much, and that the mechanism of generating them is similarly maintained over the large Richardson numbers. This is also in good agreement with Smyth and Moum [14], who reported that the CGFs appear over the dissipation range associated with the Kolmogorov scale.

Although the persistent CGFs appearing in the cospectrum are well discussed in Smyth and Moum [14], their association with the vortical structure and the buoyancy effect on the CGFs remain unknown. To investigate how persistent CGFs are associated with the vortical structure, we conditionally averaged it from the instantaneous flow field.

The vortical structure is identified by the second invariant of the deformation tensor defined as $II = -\partial u_i/\partial x_j \partial u_j/\partial x_i$, which is also represented by the strain rate and vorticity as

$$II = \tfrac{1}{2}\omega_i\omega_i - s_{ij}s_{ji}. \tag{8}$$

It is well known that the cores of the vortices correspond well to the regions $II > 0$ [3] in wall turbulence as well as to those in homogeneous shear flow. This is due to the kinematics of vortices, which dictate that a vorticity must be larger than the strain rate in the core of the vortex.

The details of the numerical procedure are the same as those used in Iida et al. [4], and are summarized as follows: (1) detection of the local maximum of the second invariant II in cross streamwise planes (positive II is used to identify the vortical structure, while the streamwise vorticity ω_1 is used to distinguish between structures with a different sense of rotation); (2) linking the local maximum of II as the core of the longitudinal vortex; (3) when the local maximum point of II in the cross-streamwise plane shifts by more than 2 grid points from the cross-streamwise plane of the previous step, the structure is considered to be terminated, and detection of a new vortical structure begins; (4) each vortex must have a streamwise length greater than $1/13L_1$, which is approximated as the integral scale $L_{11,1}$ at $St = 6$ (the condition required to capture fully developed longitudinal vortices); and (5) the educed vortical structures are averaged with the sense of rotation by aligning the midpoint of their streamwise extent. The number of vortical structures educed is about two hundreds (clockwise and anticlockwise vortices) in all cases. Almost the same number of clockwise and anticlockwise vortices is detected in RDT as in DNS.

Fig. 8 shows a top view of the three-dimensional vortical structure. As discussed in our previous study [4], the tilt in the spanwise direction is clearly observed; the vortical structure with a different sense of the streamwise vorticity is tilted in the opposite direction. Such tilting is definitely observed in the longitudinal vortical structure of near-wall turbulence [20], indicating the strong

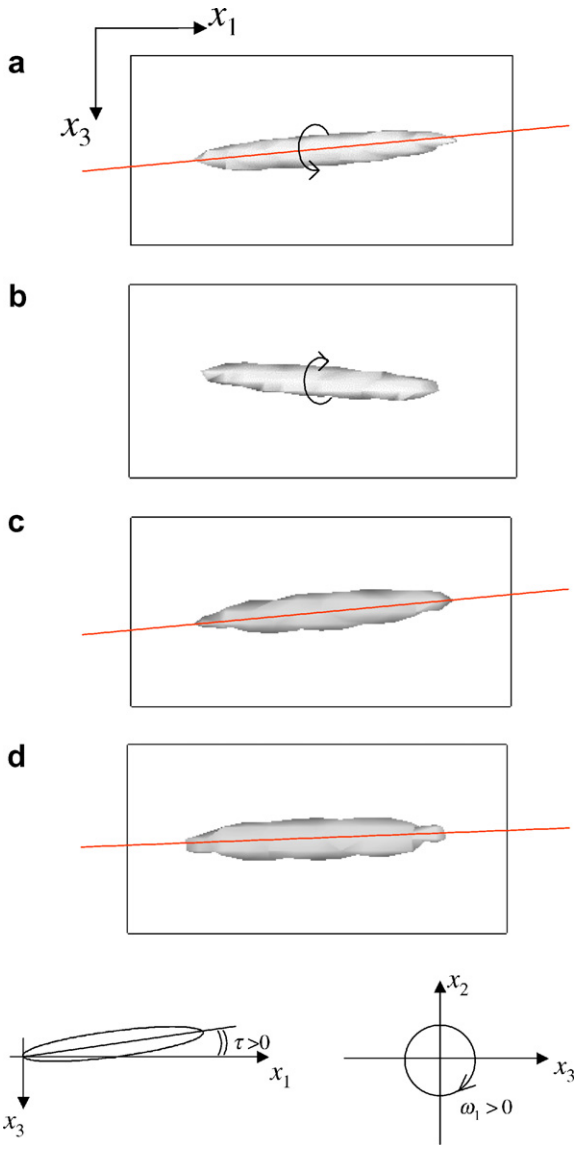

Fig. 8. Top view of isosurface of conditionally averaged vortical structure at different Richardson numbers, $II/II_{\text{r.m.s.}} = 2.0$, (a) $Ri = 0$ ($\omega_1 > 0$), (b) $Ri = 0$ ($\omega_1 < 0$), (c) $Ri = 0.4$ ($\omega_1 > 0$), (d) $Ri = 0.5$ ($\omega_1 > 0$). Sides of rectangular region are $62\sqrt{2\nu/S}$ and $31\sqrt{2\nu/S}$ in the x_1 and x_2 directions, respectively. The arrows in (a) and (b) represent the sense of rotational motion.

similarity of the vortical structure among turbulent shear flows.

During the transition to turbulence in the boundary layer, longitudinal vortices with a larger tilting angle appear in the more downstream regions [21]. It is also well known that oscillating the wall in a spanwise direction changes the tilting angle of the longitudinal vortex [22], resulting in a decrease in the skin friction coefficient. Iida et al. [4] showed that tilting is due to the nonlinear term, and hence cannot be observed in the RDT. Note that in Fig. 8 no definite qualitative change at $Ri = 0.4$ can be seen in the vortical structure. At $Ri = 0.5$, however, the tilting markedly decreases in comparison to $Ri = 0$ and 0.4, indicating an attenuation of the effects of the nonlinear term. The detailed tilting mechanism is discussed in Appendix A.

Finally, we discuss the association between the longitudinal vortical structure and persistent CGFs. Fig. 9 shows the distribution of $-\langle u_1\rangle\langle u_2\rangle$ at the different Richardson numbers in the cross streamwise plane, including the mid-point of a longitudinal vortical structure. $\langle u_j\rangle$ represents the fluctuating velocity conditionally averaged in the same procedure as averaging the longitudinal vortical structure. Note that in Fig. 9 DGFs appear on both sides of the vortex, while CGFs are always either on top or bottom. This distribution of the Reynolds shear stress is again clearly similar to that observed in a turbulent channel flow [20].

CGFs appear even in the case without buoyancy, and persist as long as the vortical structures are generated. Moreover, the radius (r_e) of the educed vortex, which represents the length scale of the CGFs, is about 1/12 of the side of the computational region ($r_e = L_2/12 = 16\sqrt{2\nu/S}$), and its wavenumber ($2\pi/r_e = 0.392\sqrt{S/2\nu}$) is located at about the peak of the dissipation spectrum (see Fig. 2). Hence, they must be persistent CGFs on a small scale.

With an increase in the Richardson number, DGFs on the side of the vortex markedly decrease, while persistent CGFs do not decrease as much; the CGFs increase spatially, and a quarter of the area becomes CGFs at $Ri = 0.5$. This is in good agreement with E_{12} shown in Fig. 7. There are, however, marked differences between RDT and DNS even at $Ri = 0.5$, indicating that the nonlinear term still works in the momentum transfer. In what follows, we will compare the case of $Ri = 0$ with that of $Ri = 0.5$ which showed significant stratified effects.

The time development of $-\langle u_1\rangle\langle u_2\rangle$ is shown in Figs. 10 and 11. In comparison to the DGFs on the vortex sides, the CGFs cannot be observed at the early period of the calculation. In time they appear, which is again in good agreement with the time development of E_{12}, and indicates that the CGFs at higher wavenumbers correspond to those at the vortex top and bottom. In the case of $Ri = 0$, both DGFs and CGFs are enhanced over time. On the other hand, at $Ri = 0.5$, DGFs are markedly attenuated with time, while the CGFs are enhanced in comparison to the DGFs, and most areas become the CGFs. To study the generation mechanism of CGFs, the transport mechanism of the Reynolds shear stress around the vortical structure is investigated.

Instantaneously, the non-dimensionalized transport equation of $-u_1u_2$ is written as follows:

$$-\frac{\partial u_1u_2}{\partial t} = 2u_2^2 + \frac{\partial(u_ju_1u_2)}{\partial x_j} + u_2\frac{\partial p}{\partial x_1} + u_1\frac{\partial p}{\partial x_2} - Riu_1\theta - u_1\frac{\partial^2 u_2}{\partial x_j^2} - u_2\frac{\partial^2 u_1}{\partial x_j^2}. \quad (9)$$

In the homogeneous shear flow, the non-dimensionalized Poisson equation of pressure can be written as

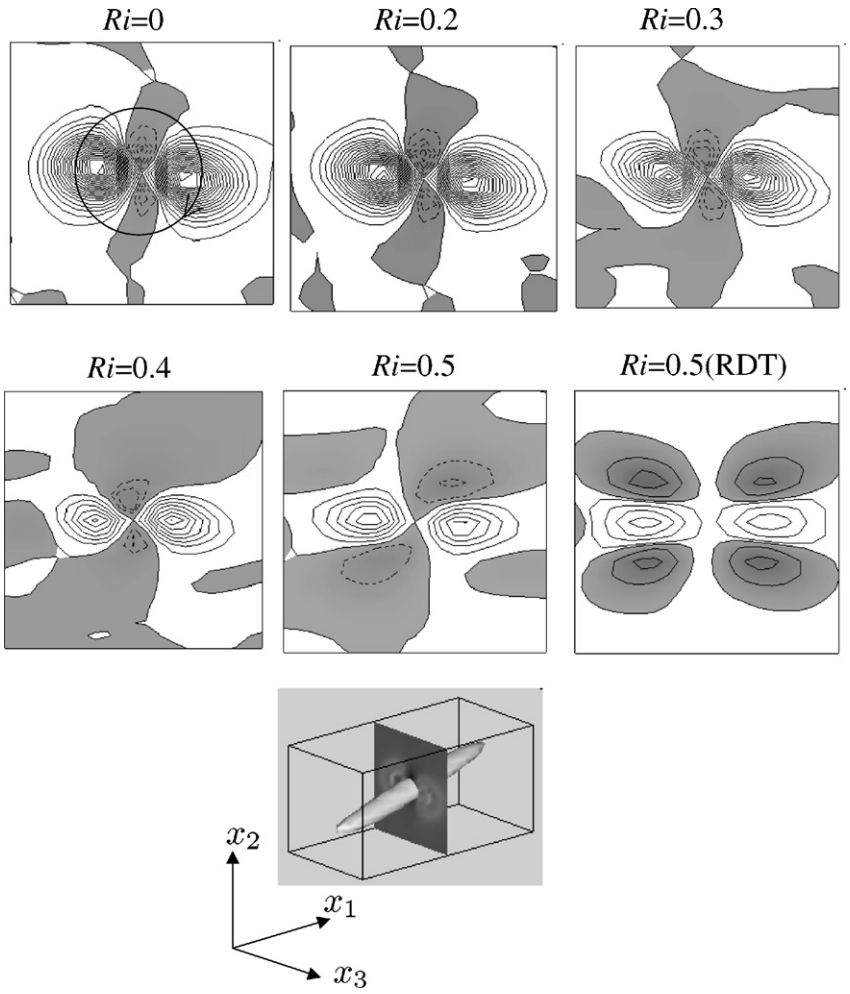

Fig. 9. Distribution of $-\langle u_1\rangle\langle u_2\rangle$ of case F3 in x_3–x_2 plane; all snapshots are at the same cross streamwise plane and at the same time ($St = 6$). Gray represents regions of $-\langle u_1\rangle\langle u_2\rangle < 0$. The contour interval is also set to be the same value 0.08 in all cases. Sides of rectangular parallelepiped including an averaged vortical structure are $62\sqrt{2\nu/S}$, $31\sqrt{2\nu/S}$, $31\sqrt{2\nu/S}$ in x_1, x_2 and x_3 directions, respectively.

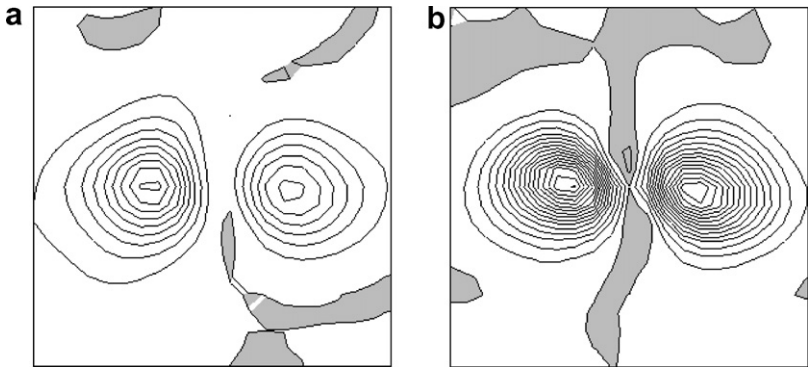

Fig. 10. Distribution of averaged Reynolds shear stress at $St = 2$ and 4 in case F3 of $Ri = 0$; both snapshots are at same cross streamwise plane as that of Fig. 9, and the contour interval is also same as that of Fig. 9.

$$\nabla^2 p = -\frac{\partial u_j}{\partial x_i}\frac{\partial u_i}{\partial x_j} - 4\frac{\partial u_2}{\partial x_1} + Ri\frac{\partial \theta}{\partial x_2}. \tag{10}$$

Moreover, the pressure can be divided into two parts, i.e., the slow and rapid pressure terms, which can be defined as

$$\nabla^2 p_r = -4\frac{\partial u_2}{\partial x_1} + Ri\frac{\partial \theta}{\partial x_2}, \tag{11}$$

$$\nabla^2 p_s = -\frac{\partial u_j}{\partial x_i}\frac{\partial u_i}{\partial x_j}. \tag{12}$$

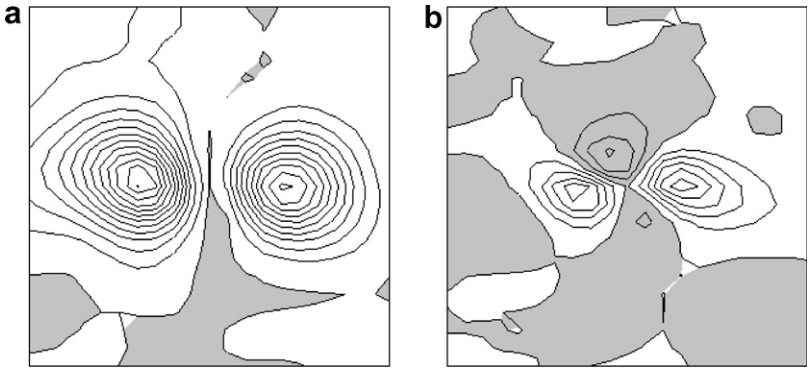

Fig. 11. Distribution of averaged Reynolds shear stress at $St = 2$ and 4 in case F3 of $Ri = 0.5$; both snapshots are at same cross streamwise plane as that of Fig. 9.

By using p_r and p_s, the transport equation of $-u_1u_2$ can be modified as follows:

$$-\frac{\partial u_1u_2}{\partial t} = 2u_2^2 + \frac{\partial(u_ju_1u_2)}{\partial x_j} + \frac{\partial}{\partial x_1}(p_su_2) + \frac{\partial}{\partial x_2}(p_su_1) - p_s\left(\frac{\partial u_2}{\partial x_1} + \frac{\partial u_1}{\partial x_2}\right) + u_2\frac{\partial p_r}{\partial x_1} + u_1\frac{\partial p_r}{\partial x_2} - Riu_1\theta - u_1\frac{\partial^2 u_2}{\partial x_j^2} - u_2\frac{\partial^2 u_1}{\partial x_j^2}, \quad (13)$$

where the last two terms representing the viscous term are small in comparison to the other terms.

In the averaged vortical structure, each term in the transport equation can be defined as follows:

$$\text{Production term} = 2\langle u_2\rangle^2, \quad (14)$$

$$\text{Turbulent diffusion term} = \frac{\partial(\langle u_j\rangle\langle u_1\rangle\langle u_2\rangle)}{\partial x_j}, \quad (15)$$

$$\text{Pressure diffusion term} = \frac{\partial}{\partial x_1}(\langle p_s\rangle\langle u_2\rangle) + \frac{\partial}{\partial x_2}(\langle p_s\rangle\langle u_1\rangle), \quad (16)$$

$$\text{Pressure strain term} = -\langle p_s\rangle\left\langle\frac{\partial u_2}{\partial x_1}\right\rangle - \langle p_s\rangle\left\langle\frac{\partial u_1}{\partial x_2}\right\rangle, \quad (17)$$

$$\text{Velocity rapid pressure gradient term} = \langle u_2\rangle\left\langle\frac{\partial p_r}{\partial x_1}\right\rangle + \langle u_1\rangle\left\langle\frac{\partial p_r}{\partial x_2}\right\rangle, \quad (18)$$

$$\text{Buoyancy term} = -Ri\langle u_1\rangle\langle\theta\rangle, \quad (19)$$

$$\text{Viscous term} = -\langle u_1\rangle\left\langle\frac{\partial^2 u_2}{\partial x_j^2}\right\rangle - \langle u_2\rangle\left\langle\frac{\partial^2 u_1}{\partial x_j^2}\right\rangle. \quad (20)$$

Except for pressure, these definitions are the same as those in [3], where each budget term is visualized in a turbulent channel flow performed by DNS. In this study, however, slow pressure is used to define both pressure–strain and pressure–diffusion terms, while the velocity-rapid-pressure-gradient term is calculated separately.

Slow pressure is associated with the vortical structure, and is known to be dominant in comparison to the rapid term in near-wall turbulence [23], while in a homogeneous shear flow mostly predicted by the RDT, the rapid term cannot be negligible. Hence, it is better to separate the pressure when comparing the details of the momentum transfer between near-wall turbulence and homogeneous shear flow.

Fig. 12 shows the velocity vectors and each of the budget terms at $Ri = 0$ in case F3. In the velocity vectors, vortical motion is clearly observed, indicating that the isosurface of II represents the streamwise vortex. It should also be noted that the production term appears on the sides of the vortex, from where the turbulent-diffusion term transfers the Reynolds shear stress to the top and bottom of the vortex. The pressure–diffusion term transfers from the outside of the vortex to the inside where the pressure–strain term contributes to a drop in the Reynolds shear stress. The above mentioned transport mechanism is very similar to the one observed in a turbulent channel flow (see [3]).

Fig. 13(a) and (b) shows the balances of the budget terms at $Ri = 0$. Note that at $Ri = 0$, the sum of the turbulent-diffusion and production terms assumes definite negative values at the top and bottom where persistent CGFs appear, but positive values at the vortex sides where DGFs assume the maximum value, indicating that both the DGFs and the persistent CGFs are associated with the sum of the production and turbulent-diffusion terms. The total balance of the Reynolds shear stress, i.e., the sum of all terms in Eqs. (14)–(20), is virtually identical to the sum of the production and turbulent-diffusion terms (see Fig. 13(b)). Hence, both the CGFs and the DGFs must increase with time as previously shown.

Fig. 14 shows the velocity vectors and each budget term at $Ri = 0.5$ in case F3. In the velocity vectors, the vortex in the center of the figure becomes a horizontally elongated and vertically compressed structure. Interestingly, this vortex is flanked by other streamwise vortices at both top and bottom. The transport mechanism in the case of $Ri = 0.5$ is, however, qualitatively similar to that in the case without stratification; no definite effects of buoyancy are observed except the buoyancy and velocity-rapid-pressure-gradient

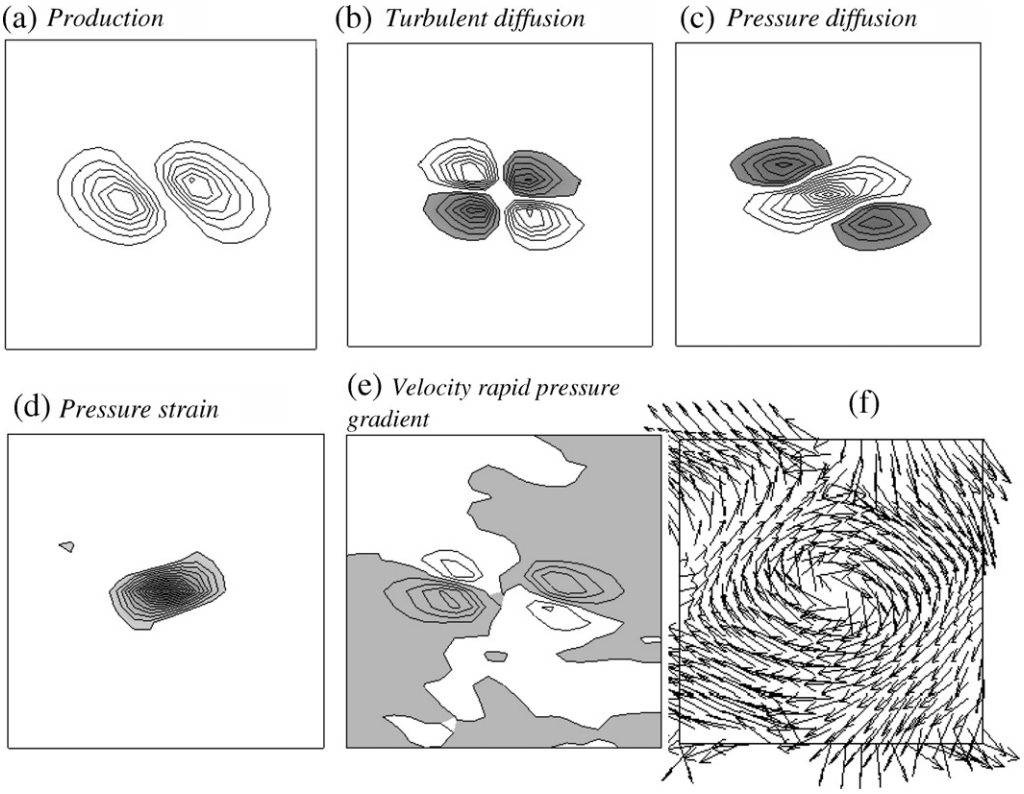

Fig. 12. Distribution of budget terms in case F3 of $Ri = 0$. All snapshots are at same cross streamwise plane and same time as those of Fig. 9. (a) Contours of production term from 0.1 to 0.7, (b) contours of turbulent-diffusion term from −0.6 to −0.1 and from 0.1 to 0.7, (c) contours of pressure–diffusion term (slow term) from −0.5 to −0.1 and from 0.1 to 0.9, (d) contours of pressure–strain term (slow term) from −1.4 to −0.1, (e) contours of rapid-pressure–velocity-gradient term from −0.2 to 1.0 with the interval of 0.5, (f) velocity vectors. The contour interval is set to be 0.1 in all the budget terms except rapid-pressure–velocity-gradient term.

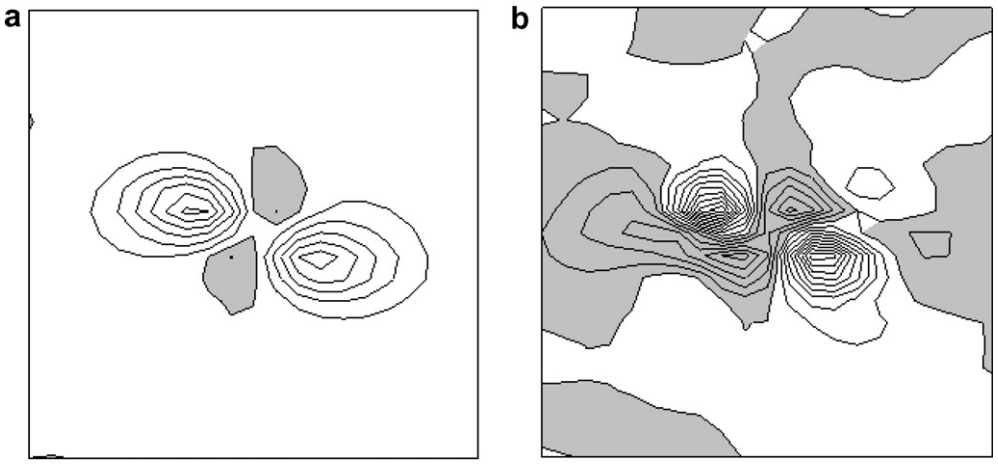

Fig. 13. Balance of budget terms at $St = 4$ of case F3 at same cross streamwise plane as that of Fig. 9. (a) Balance of production and turbulent-diffusion terms of $Ri = 0$ from −0.5 to 3.0 with the interval of 0.5, (b) balance of all the budget terms of $Ri = 0$ from −1.0 to 1.8 with the interval of 0.2.

terms. Interestingly, the rapid-pressure term works to reduce the effects of the buoyancy term, which assumes a strongly negative value at both vortex sides, and must decrease the DGFs there. Moreover, the buoyancy term, transported around the vortex, takes a strong negative value in both the vortex top and bottom, which must be due to the swirling motion and obviously nonlinear phenomena. Thus, the buoyancy term must increase the CGFs, though it attenuates the DGFs.

In short, the persistent CGFs are generated by both the production and turbulent-diffusion terms, and enhanced by the buoyancy term, so that they do not decrease as much

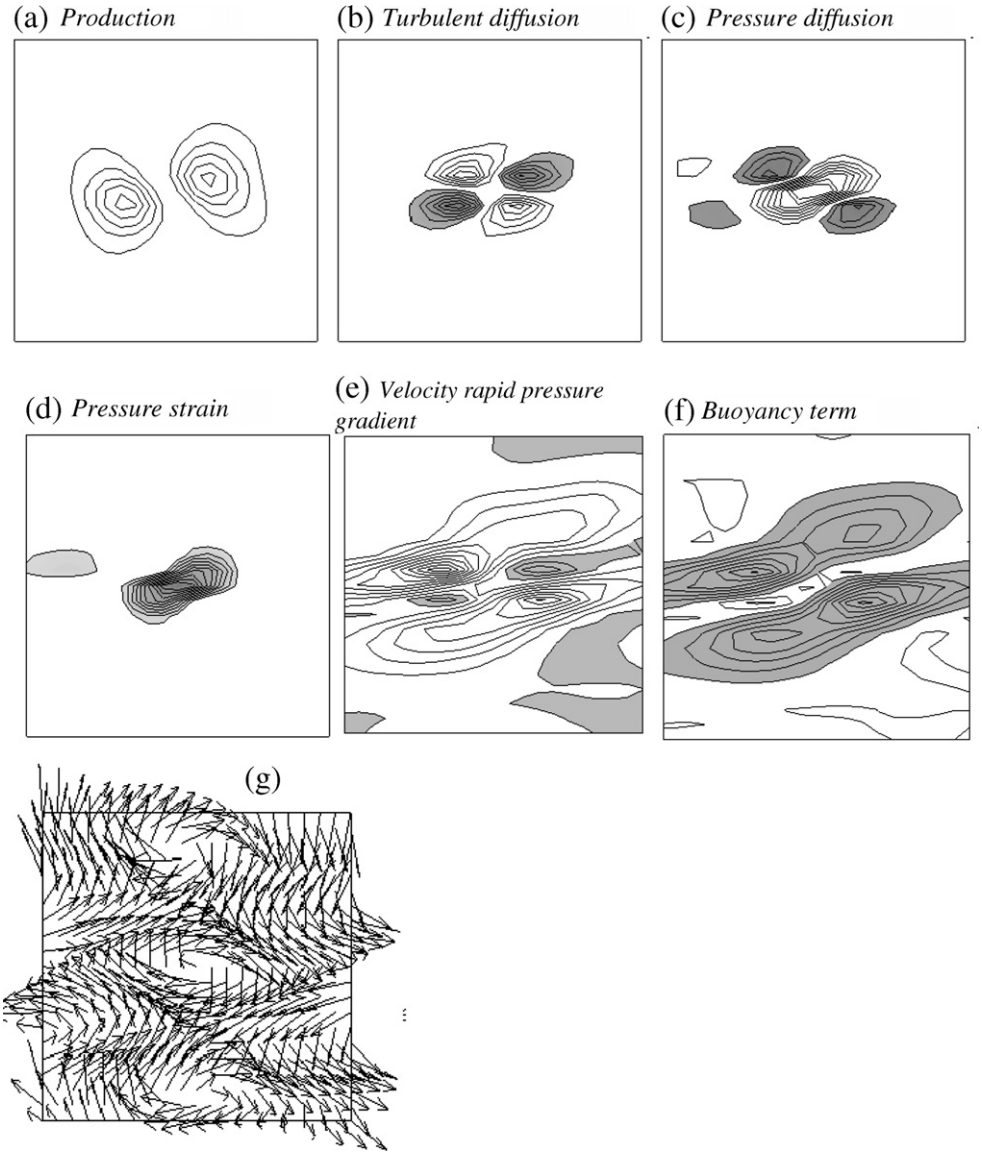

Fig. 14. Distribution of budget terms in case F3 of $Ri = 0.5$; all snapshots are at same cross streamwise plane and same time as those of Fig. 9. (a) Contours of production term from 0.04 to 0.2, (b) contours of turbulent-diffusion term from −0.24 to −0.04 and from 0.04 to 0.14, (c) contours of pressure–diffusion term (slow term) from −0.16 to −0.04 and from 0.04 to 0.32, (d) contours of pressure–strain term (slow term) from −0.4 to 0.04, (e) contours of rapid-pressure–velocity-gradient term from −0.1 to 0.5 with the interval of 0.05, (f) contours of buoyancy term from −0.45 to 0.05 with the interval of 0.05, (g) velocity vectors. The contour interval is set to be 0.04 in all the budget terms except rapid-pressure–velocity-gradient and buoyancy terms.

as the DGFs, and hence increase spatially with an increase in the Richardson number.

4. Conclusions

Direct numerical simulations of homogeneous shear flow under stable-density stratification are performed to study the buoyancy effects on both the transport mechanism and vortical structure. In all cases, the Prandtl number of the fluid is 0.71 by assuming the air flow, and hence the effects of the different Prandtl number are beyond scope of our study. The numerical data obtained are compared with those of a turbulent channel flow under stable stratification and other homogeneous shear flows, to show the similar buoyancy effect among different flows. The mechanism of persistent CGFs is also studied in their association with the vortical structure.

(1) The stationary values of both R_{12} and $R_{2\theta}$ are obtained at the stationary Richardson number determined by the time development of turbulent kinetic energy. The plots of R_{12} and $R_{2\theta}$ versus the Richardson number are quantitatively in good agreement with those of stably stratified channel flow.
(2) The visualization of turbulent structures shows that there is a close association between the streamwise

vortical structure and the persistent CGFs, which appear at the top and bottom of the vortex. With an increase in the Richardson number, the Reynolds shear stress at the sides of the vortex markedly decreases, while the persistent CGFs do not decrease as much as the Reynolds shear stress, and the area of the CGFs increases.

(3) The transport mechanism of the Reynolds shear stress was investigated around the vortical structure. It was found that the production of the Reynolds shear stress takes a large value on both sides of the vortex, and that the turbulent diffusion transfers it around the vortex sphere, while pressure diffusion transfers it to the inside of the vortex where the pressure–strain correlation destroys it. The above-mentioned transport mechanism is surprisingly similar to that in the turbulent channel flow. It was also found that the sum of the turbulent-diffusion and production terms corresponds well to the Reynolds shear stress. Hence, their sum is mostly responsible for both CGFs and DGFs. With an increase in the Richardson number, the negative regions of the buoyancy term expand from the vortex sides to its top and bottom by a swirling motion, and hence the CGF regions expand.

Acknowledgements

This work was supported by the Ministry of Education, Culture, Sports, Science, and Technology through a Grant-in-Aid for Scientific Research (No. 16760153), and by the Toyota Physical and Chemical Research Institute. The authors are deeply grateful to Prof. K. Suzuki, Editor of IJHMT and anonymous referees for the valuable comments on this manuscript.

Appendix A

In this appendix, we discuss the relation between the tilting and strain-rates imposed on the vortex. Figs. 15 and 16 show the association between tilting angle τ and strain rate $\partial u_\alpha/\partial x_\alpha$ in the averaged longitudinal vortical structure of $\omega_1 > 0$. As shown in Fig. 8, the tilting angle is determined as the angle between the x_1 axis and the segment connecting the cores of vortices at both edges of a longitudinal vortical structure, while the strain rate at the vortex core is averaged over the vortex axis to reduce fluctuations, and normalized by each r.m.s. value.

In the case without buoyancy, the dots of the tilting angle are unevenly distributed on the right-hand side, indicating that most vortices with positive streamwise vorticity

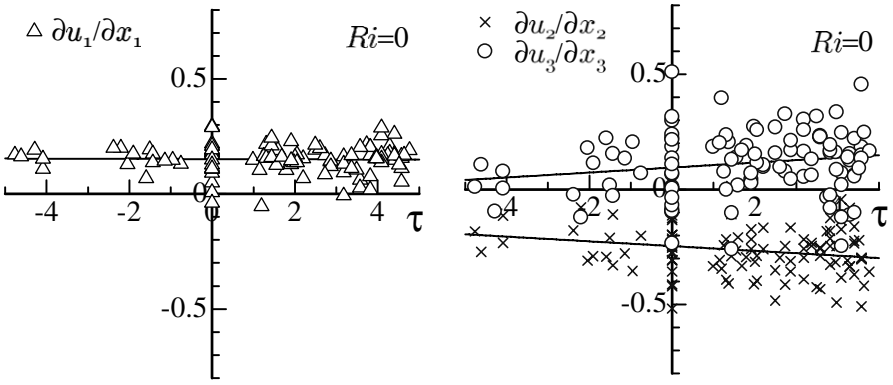

Fig. 15. Correlation between tilting angle and strain rates at $Ri = 0$.

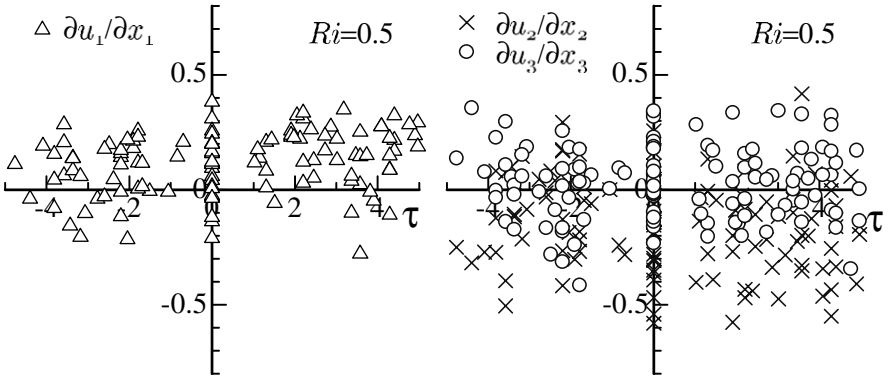

Fig. 16. Correlation between tilting angle and strain rates at $Ri = 0.5$.

have a positive tilting angle. It is also found that in the vortex core, the strain rates $\partial u_1/\partial x_1$ and $\partial u_3/\partial x_3$ are positive, whereas the rate $\partial u_2/\partial x_2$ is negative. Moreover, an increase in the tilting angle is almost proportionate to that of $|\partial w/\partial z|$ and $|\partial v/\partial y|$, though no correlation can be seen between the tilting angle and $|\partial u/\partial x|$.

In the case of $Ri = 0.5$, the dots of the strain rates are more scattered, though $\partial u_1/\partial x_1$ and $\partial u_2/\partial x_2$ still tend to be positive and negative, respectively. However, a marked difference is observed on $\partial u_3/\partial x_3$ between $Ri = 0$ and 0.5; the dots of $\partial u_3/\partial x_3$ are evenly distributed between the upper (positive) and the lower (negative) regions in the case of $Ri = 0.5$, indicating that the vortex stretching in the spanwise direction becomes essentially negligible. Hence, the spanwise stretching must be associated with the tilting of the longitudinal vortex in a spanwise direction.

References

[1] D.J. Tritton, Physical Fluid Dynamics, The Oxford University Press, 1988, p. 197.

[2] S.K. Robinson, The kinematics of turbulent boundary layer structure, NASA TM-103859, 1991.

[3] N. Kasagi, Y. Sumitani, Y. Suzuki, O. Iida, Kinematics of the quasi-coherent vortical structure in near-wall turbulence, Int. J. Heat Fluid Flow 16 (1995) 2–10.

[4] O. Iida, M. Iwatsuki, Y. Nagano, Vortical turbulence structure and transport mechanism in a homogeneous shear flow, Phys. Fluids 12 (2000) 2895–2905.

[5] C.A.G. Webster, An experimental study of turbulence in a density stratified shear flow, J. Fluid Mech. 19 (1964) 221–245.

[6] T. Gerz, U. Schumann, S.E. Elghobashi, Direct numerical simulation of stratified homogeneous turbulent shear flows, J. Fluid Mech. 200 (1989) 563–594.

[7] J.I. Rohr, E.C. Itsweire, K.N. Helland, C.W. Van Atta, Growth and decay of turbulence in a stably stratified shear flow, J. Fluid Mech. 195 (1988) 77–111.

[8] H. Hanazaki, J.C.R. Hunt, Linear processes in unsteady stably stratified turbulence, J. Fluid Mech. 202 (1996) 303–337.

[9] S.E. Holt, J.R. Koseff, J.H. Ferziger, A numerical study of the evolution and structure of homogeneous stably stratified turbulence, J. Fluid Mech. 237 (1992) 499–539.

[10] T.G. Gerz, U. Schumann, A possible explanation of counter gradient fluxes in homogeneous turbulence, Thoret. Comput. Fluid Dynam. 8 (1996) 169–181.

[11] S.P.S. Piccirillo, C.W. Van Atta, The evolution of a uniformly sheared thermally stratified turbulent flow, J. Fluid Mech. 195 (1997) 61–86.

[12] D.J. Tritton, Physical Fluid Dynamics, The Oxford University Press, 1988, p. 309.

[13] R. Antonia, M. Teitel, J. Kim, L. Browne, Low-Reynolds-number effects in a fully developed turbulent channel flow, J. Fluid Mech. 236 (1992) 579.

[14] W.D. Smyth, J.N. Moum, Anisotropy of turbulence in stably stratified mixing layers, Phys. Fluids 12 (2000) 1343–1363.

[15] S. Rogallo, Numerical experiments in homogeneous turbulence, NASA TM-81315, 1981.

[16] L.H. Shih, J.R. Koseff, J.H. Ferziger, C.R. Rehmann, Scaling and parameterization of stratified homogeneous turbulent shear flow, J. Fluid Mech. 412 (2000) 1–20.

[17] F.G. Jacobitz, S. Sarkar, C.W. Van Atta, Direct numerical simulations of the turbulence evolution in a uniformly sheared and stably stratified flow, J. Fluid Mech. 342 (1997) 231–261.

[18] O. Iida, N. Kasagi, Y. Nagano, Direct numerical simulation of turbulent channel flow under stably density stratification, Int. J. Heat Mass Transfer 45 (2002) 1693–1703.

[19] S. Komori, H. Ueda, F. Ogino, T. Mizushina, Turbulence structure in stably stratified open-channel flow, J. Fluid Mech. 130 (1983) 13–26.

[20] J. Jeong, F. Hussain, W. Schoppa, J. Kim, Coherent structures near the wall in a turbulent channel flow, J. Fluid Mech. 332 (1997) 185–214.

[21] L. Brandt, D.S. Henningson, Transition of streamwise streaks in zero pressure-gradient boundary layers, J. Fluid Mech. 472 (2002) 229–261.

[22] A.T. Le, G.N. Coleman, J. Kim, Near-wall turbulence structures in three-dimensional boundary layers, Int. J. Heat Fluid Flow 21 (2000) 480–488.

[23] J. Kim, P. Moin, R. Moser, Turbulence statistics in fully developed channel flow at low Reynolds number, J. Fluid Mech. 177 (1987) 133–166.